Journal of Alloys and Compounds 863 (2021) 158339

Contents lists available at ScienceDirect

Journal of Alloys and Compounds

journal homepage: www.elsevier.com/locate/jalcom

Oxygen migration induced effective magnetic and resistive switching boosted by graphene quantum dots

Shuxia Ren[a], Zhenhua Li[a], Xiaomin Liu[a], Yongsheng Li[b], Guozhong Cao[c,*], Jinjin Zhao[a,*]

[a] School of Materials Science and Engineering, School of Mechanical Engineering, Shijiazhuang Tiedao University, Shijiazhuang 050043, China
[b] Lab of Low-Dimensional Materials Chemistry, Key Laboratory for Ultrafine Materials of Ministry of Education, School of Materials Science and Engineering, East China University of Science and Technology, Shanghai 200237, China
[c] Department of Materials Science and Engineering, University of Washington, Seattle, WA 98195-2120, USA

ARTICLE INFO

Article history:
Received 8 November 2020
Received in revised form 9 December 2020
Accepted 13 December 2020
Available online 9 January 2021

Keywords:
Graphene oxide
Graphene quantum dots
Resistive memory
Magnetic modulation

ABSTRACT

Graphene materials have attracted considerable research interest owing to their applications in memristor and prospective spintronic devices. In this work, the bifunctional resistive and magnetic switching effect is investigated in Ag/graphene quantum dots (GQDs): graphene oxide (GO)/ITO device: (1) In the low-resistance state, the conductive filaments are formed by oxygen migration away inducing the C–C sp^2 groups. (2) In the high-resistance state, the directions of magnetic moment align by increasing the C–O sp^3 group. The resistive switching ratios and saturation magnetization of GQDs memristor are shown to be approximately 20 and 2.2 times higher than that of GQDs-free memristor, respectively. Tunable magnetic switching makes GO-based memristive devices boosted by GQDs a promising candidate to future voltage-controlled, low-power, and high-density spintronics devices.

1. Introduction

Resistive random-access memories (RRAMs), as one of the most promising next-generation information storage technologies, have attracted a lot of attention owing to their simple structure, fast speed, and low power consumption [1–4]. The resistive switching (RS) behaviour exhibits non-volatility under the application of an electric field [5]. Recently, the control of non-volatile magnetism by using an electric field during the RS process has been observed in many oxide films [5–8], and it provides a promising avenue for combining charge and spin manipulations to produce novel spintronic devices [9]. The significant potential applications of graphene-based spintronic devices are promising, owing to their weak spin-orbit coupling, long spin diffusion lengths and coherence times, and extraordinary carrier mobility [10–12]. Various magnetic properties were recently reported in graphitic compounds [13–16] with layered structures, such as graphite. Graphene oxide (GO) is a typical semiconductor, which can be modified with oxygen groups such as epoxy (C–O–C), carbonyl (C=O), and hydroxyl (–OH), along the basal plane and edges [17–20]. This structure equips GO with excellent optical, thermal, and dielectric properties, and also facilitates the mass production of graphene through reduction [21–23]. Notably, magnetism has been predicted in GO, and many investigations have suggested that the magnetic properties originate from oxygen groups [24–30]. Tang et al. [24] identified the magnetic properties of GO by controlling the oxidation degrees. Lee et al. [14,30] suggested that the unpaired spin in certain carbon atoms, induced by the surrounding epoxy groups, produced a magnetic moment. It was apparent that the number of oxygen groups played a fundamental role in the observed magnetism. Most importantly, the electrical properties of GO could be modulated by the RS behaviour [31–36]. It was reported that the formation of graphitic filaments (highly conductive paths connected by sp^2 clusters), induced by the migration of oxygen anions upon the application of an external field, could be considered as an RS mechanism in GO films [37,38]. Sp^2 graphitic nano-filaments with conical shapes were observed using in-situ transmission electron microscopy (TEM) techniques [39]. As the movement of oxygen anions has an extremely important effect on the RS behaviour of GO films, the number of oxygen groups in GO is closely related to its magnetism. Therefore, it is plausible to manipulate, as well as improve, the magnetism of GO films by controlling their RS effect under an applied electric field, which can make GO an excellent material for spintronic and non-volatile-memory-based bifunctional device applications.

Graphene quantum dots (GQDs), being edge-functionalized nanometre-sized graphene fragments [40–44], possess unique electronic properties [44,45] owing to the quantum confinement and

* Corresponding authors.
E-mail addresses: gzcao@u.washington.edu (G. Cao), jinjinzhao2012@163.com (J. Zhao).

https://doi.org/10.1016/j.jallcom.2020.158339
0925-8388/

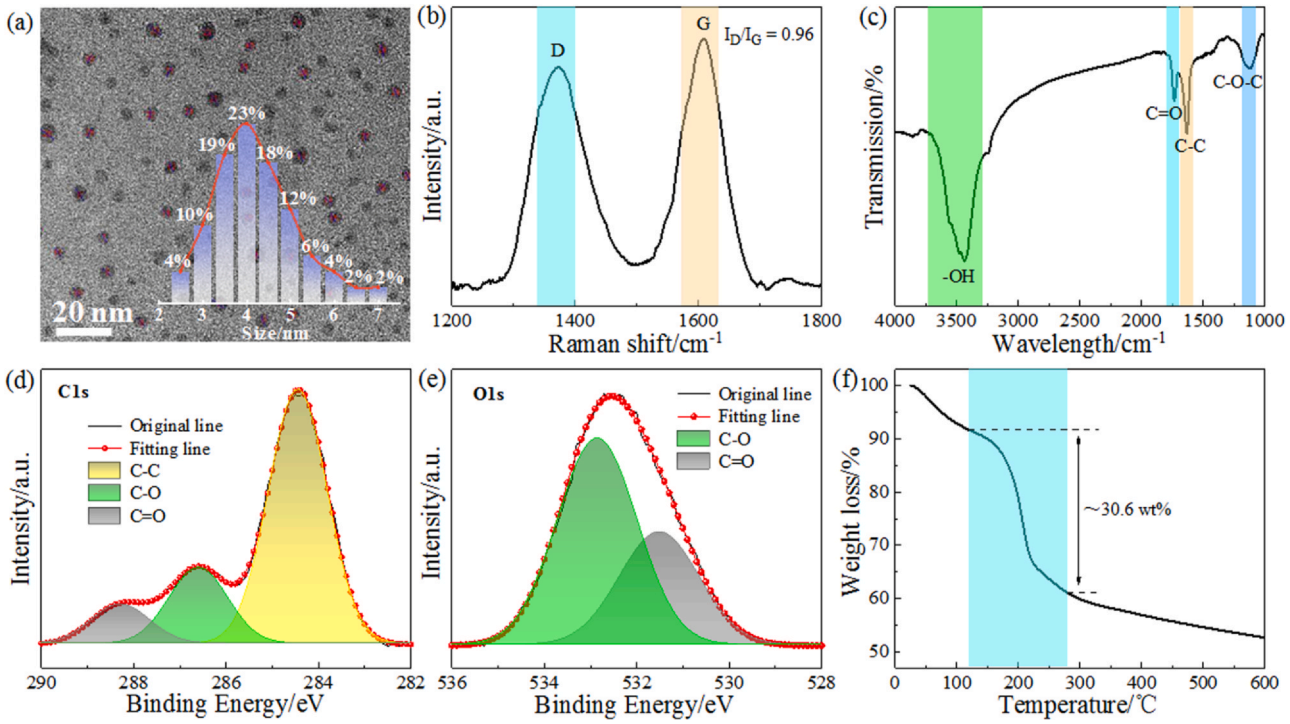

Fig. 1. Characterization of the as-received GQDs. (a) TEM image. The inset shows the size distribution. (b) Raman spectrum. (c) FT-IR spectrum. (d) High-resolution C1s XPS spectrum. (e) High-resolution O1s XPS spectrum. (f) TGA profile.

edge effects [44,46,47]. They can enhance the local electric field to guide the growth directions of conductive filaments (CFs) to provide superior uniformity of RS properties [40,44,48]. But so far, there is no report related to the effect of GQDs on the resistive and magnetic switching behaviour of GO film. In this work, we prepared bifunctional GO-based RRAMs with enhanced RS behaviour and magnetic properties at low operating voltages by incorporating GQDs with 8 wt% into the GO film. The GQDs not only contributed to excellent RS characteristics such as centralized SET and RESET voltages, large RS ratios, and superior reliability, but also helped connect magnetic moments between GO layers when the RS dielectric layer is in the high-resistance state (HRS), and thereby improved the global magnetic behaviour at room temperature.

2. Methods

2.1. Materials

GQD nanoparticles and GO suspension (2 mg/mL) were obtained from Nanjing XFNANO Materials Tech. Co., Ltd. The indium-tin oxide (ITO with the sheet resistance of 15 ± 2 Ω sq^{-1} and thickness of approximately 120 nm)-coated polyethylene terephthalate (PET) substrate was purchased from Liaoning Advanced Election Technology Co., Ltd.

2.2. Fabrication of Ag/GQDs:GO/ITO device

GQDs were added to a GO suspension through ultrasonic dispersion in a water bath at 25 °C for 40 min. The weight ratio of GQDs in the suspension was 8%. The resultant mixture suspension was then spin-coated, at 300 rpm and 2000 rpm for 20 s and 60 s, respectively, on a commercial ITO-PET to obtain GQDs:GO hybrid films by annealing at 100 °C for 60 min in air. Ag with a thickness of approximately 100 nm [49,50] was deposited as top electrode (TE) [51] on the surface of the hybrid film to form an Ag/GQDs:GO/ITO device using thermal evaporation with a shadow mask. For purposes of comparison, the Ag/GO/ITO sandwich structure without the GQDs was produced as a control memory using the same process.

2.3. Characterization

The morphology and structure of the samples were characterized through TEM (JEOLJEM2010), scanning electron microscopy (SEM, Hitachi S-4800) with energy-dispersive spectroscopy (EDS, EDAX E1506-C2B), Fourier transform infrared spectrometry (FT-IR, 8400 S Shimadzu), Raman spectroscopy (Yvon-Horiba T64000), thermogravimetric analysis (TGA, Mettler-Toledo) with heating from 25° to 600 °C at 10 °C min^{-1}, and X-ray diffraction (XRD, X′pert PRO MPD). The chemical states of the elements were analyzed using X-ray photoemission spectroscopy (XPS, PHI5000 Versa Probe) with a C1s peak of carbon contamination at 284.8 eV. The energy bands of GO and GQDs were determined with ultraviolet photoelectron spectroscopy (UPS, Thermo ESCALAB 250XI) with a He I (21.22 V) radiation source and ultraviolet-visible absorption spectra (UV–Vis, TU-1901) in the wavelength range of 200–700 nm. The RS characteristics were measured at room temperature with a Keithley 2612 A source meter. The magnetic hysteresis (*M-H*) curves at room temperature were obtained using a magnetic-property measurement system (MPMS, Quantum Design, Inc.) with a magnetic field applied in the in-plane direction.

3. Results and discussion

The TEM image shown in Fig. 1(a) indicates that the as-received GQDs are monodispersed with a size of 4.23 ± 0.21 nm (inset of Fig. 1a). Fig. 1(b) displays the Raman spectrum of the GQDs: a disordered (D) peak representing sp^3 bonding defects and a crystalline (G) peak representing sp^2 carbon [38] appear clearly at the centre of 1373 cm^{-1} and 1608 cm^{-1}, respectively. The value of the peak intensity ratio between D band and G band, I_D/I_G is 0.96, indicating that there are massive structural defects, mainly oxygen groups, in the GQDs [44,52,53]. This is further confirmed by the FT-IR spectrum

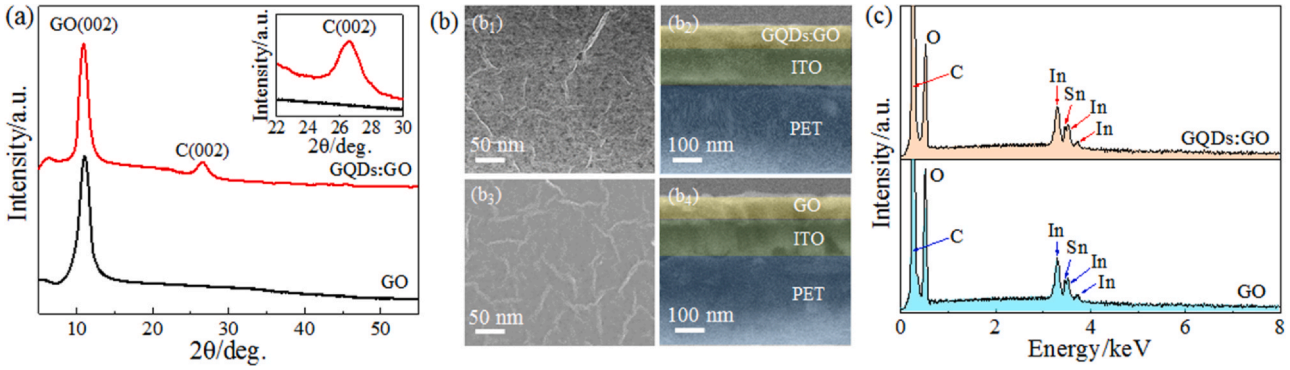

Fig. 2. Characterization of GQDs:GO hybrid film and GO film. (a) XRD pattern. The inset shows a partial enlarged view. (b) Top view SEM images (b_1 and b_3) and cross-sectional SEM (b_2 and b_4). (c) SEM–EDS spectra.

shown in Fig. 1(c). The oxygen groups, including epoxide (C–O–C), carbonyl (C=O), and hydroxyl (–OH) [44,52], exist in the GQDs. Only C1s and O1s signals were detected in the XPS analysis, without any other impurities in the GQDs (see Fig. S1 in the Supporting Information). The corresponding high-resolution C1s and O1s XPS spectra are shown in Fig. 1(d) and (e), respectively. The C1s spectrum can be subdivided into three peaks at approximately 284.4, 286.5, and 288.3 eV, attributed to the C–C (sp^2), C–O (epoxide), and C=O (carbonyl), respectively [54–56].

The relative percentage of oxygen is determined to be approximately 31.2% by calculating the area of the fitting peak. The O1s spectrum indicates that oxygen mainly exists in the form of C–O (epoxide) and C=O (carbonyl) with peaks located at 532.8 and 531.5 eV [57], respectively. The thermal stability was determined by TGA for the GQDs, as shown in Fig. 1(f). A mass loss of approximately 30.6% occurs at 120–280 °C caused by the decomposition of oxygen groups [52] in the GQDs, consistent with the above C1s spectrum. In addition, the 8.2% loss below 120 °C is due to adsorbed water, which is in agreement with a predominant OH peak shown in Fig. 1(c), and the continued weight loss above 280 °C can be mainly ascribed to the carbon burning [58]. This indicates that the oxygen groups in the GQDs do not decompose at the film preparation temperature of 100 °C.

Fig. 2 compares the structures and morphologies of the GQDs:GO hybrid film and GO film. XRD patterns (Fig. 2a) reveal that, in addition to a strong peak at 2θ = 11.2° for GO film [59], the GQDs:GO hybrid film has a peak at 26.5°, which can be well indexed to graphite (002) with the standard JCPDS card (89-7213) [42,60], confirming the coexistence of GO and GQDs. This is further corroborated by the SEM analysis, as shown in Fig. 2(b). The top view SEM images show that GQD nanoparticles are homogeneously dispersed in the GQDs:GO hybrid film (Fig. 2b_1) compared with the significant wrinkles of pure GO film (Fig. 2b_3). Both films have the same uniform thickness of approximately 80 nm from the cross-sectional SEM images shown in Fig. 2(b_2) and (b_4). Fig. 2(c) shows the SEM–EDS spectra of the GQDs:GO hybrid film and GO film on ITO/PET substrate. Only C and O elements were detected in addition to In and Sn from the substrates, and those element percentages are listed in Table. S1 in the Supporting Information.

The RS performance of the Ag/GQDs:GO/ITO and Ag/GO/ITO devices are expressed in Fig. 3. The schematic configuration of the Ag/GQDs:GO/ITO device is depicted in the left inset of Fig. 3(a). All the negative and positive bias was applied on the Ag top electrode (TE) with the ITO bottom electrode (BE) grounded. The bias voltage was swept from zero → −Vmax → zero → +Vmax → zero with a compliance current (100 mA) to avoid the device being permanently broken down during the measurement. Fig. 3(a) displays the first current-voltage (*I–V*) curve of the as-fabricated Ag/GQDs:GO/ITO device. The device demonstrated forming-free bipolar RS behaviour, which is desirable for low-power-consumption devices [61,62]. The device is originally in the HRS, which is set to the low-resistance state (LRS) (termed as the SET process) when subjected to a negative bias voltage of approximately −0.43 V (SET voltage). It is subsequently reset back to the HRS again (termed as the RESET process) under a positive bias voltage of around 0.43 V (RESET voltage). The SET and RESET voltages, denoted as V_{SET} and V_{RESET}, respectively, are about 65% lower than the corresponding values of −1.24 and 1.22 V of the Ag/GO/ITO device shown in the right inset in Fig. 3(a). The corresponding *I–V* 3D plot of both the devices over 100 consecutive cycles are displayed in Fig. S3 in the Supporting Information. The histograms of the operating voltage distributions of both the Ag/GQDs:GO/ITO and Ag/GO/ITO devices over 100 switching cycles are shown in Fig. 3(b). This shows that V_{SET} and V_{RESET} of the Ag/GQDs:GO/ITO device, with the small variations of 0.06 and 0.04 V, have more centralized distributions than those of the Ag/GO/ITO device with large fluctuations, implying significantly improved uniformity of the operating voltages with GQDs. The deviation ranges shown in Fig. 3(c) for the Ag/GQDs:GO/ITO device, in both HRS (≈ 41 kΩ) and LRS (≈ 40 Ω) within 500 cycles are less obvious than those for the Ag/GO/ITO device, and the RS ratio (in the recognisable window) is greater than 10^3, which is about 20 times higher than the value of 51 for the latter device and other GO-based RS memories [54,63,64]. Moreover, the RS ratio is still more than 10^3 for the Ag/GQDs:GO/ITO device after 28 days of placement at room temperature (see Fig. 3d). The above results show that the Ag/GQDs:GO/ITO device exhibits centralized V_{SET} and V_{RESET}, high resistance ratio, and superior endurance and retention properties, which are suitable for practical device applications.

To evaluate the reliability of the device, 36 memory cells were randomly selected and switched in the Ag/GQDs:GO/ITO device. The corresponding resistance values of each memory cell in the HRS and LRS are shown in Fig. 4(a) and (b), respectively. It was found that 32 cells out of the 36 cells were functional, implying a high yield of up to 89% for the device, and the cell-to-cell variation was small. As shown in Fig. 4(c), well-defined bi-stable states were found in a vertical-bar array structure of the resistance values for each memory cell, and the RS ratio was stable at a value greater than 10^3. The operating voltages of 32 normal memory cells were counted, as shown in Fig. 4(d). The results show that both the V_{SET} and V_{RESET} dispersions are relatively centralized, only approximately 0.05 V, signifying a high reliability.

To clarify the magnetic change of the GO-based film during the RS process, the *M–H* curves of the Ag/GQDs:GO/ITO and Ag/GO/ITO devices in the initial state (IS) were first measured at room temperature (see Fig. S4 in the Supporting Information), and then re-measured after switching to LRS and HRS. The signal from the ITO/PET substrate (the bottom-right inset of Fig. S4 in the Supporting Information) has been subtracted using a method described in our

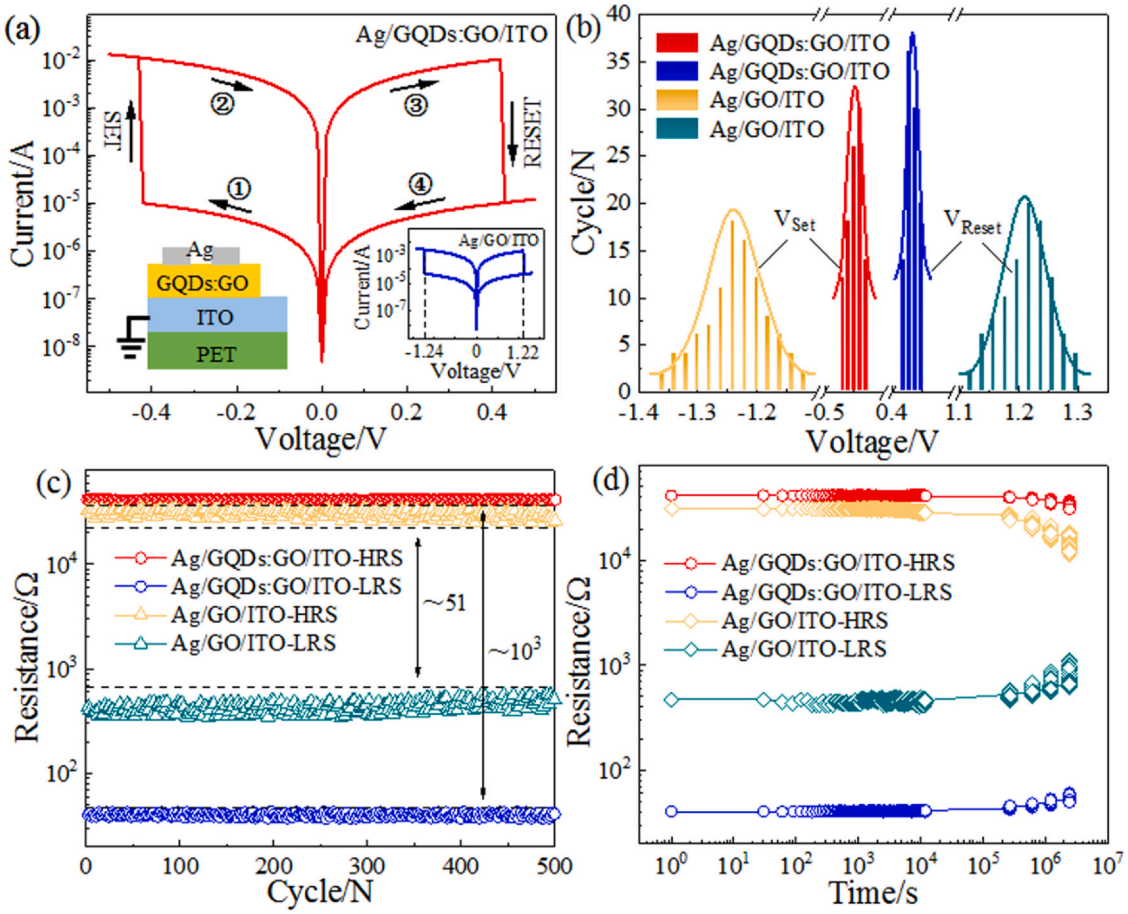

Fig. 3. RS performances of Ag/GQDs:GO/ITO and Ag/GO/ITO devices. (a) *I–V* characteristics of Ag/GQDs:GO/ITO device. The arrows indicate the voltage sweeping directions. The left inset illustrates the schematic structure of the Ag/GQDs:GO/ITO device. The right inset illustrates the *I–V* characteristics of Ag/GO/ITO device. (b) Distribution of V_{SET} and V_{RESET} over 100 switching cycles. (c) Endurance and (d) retention performance of both of Ag/GQDs:GO/ITO and Ag/GO/ITO devices, HRS and LRS read at −0.02 V.

previous work [5,65]. Fig. 5(a) displays the *M–H* curves of both the GQDs:GO hybrid and GO films in the HRS and LRS. Both films exhibit the magnetic switching behaviour and the saturation magnetization (M_s) in the HRS is greater than that in the LRS. For the GQDs:GO hybrid film, the M_s value is 4.18×10^{-3} emu cm^{-3} in the LRS, which increases significantly to 2.45×10^{-2} emu cm^{-3} when the film reset back to the HRS. The magnetic change ratio (M_{HRS}/M_{LRS}, defined as the M_s value ratio between the HRS and LRS) is 5.86, much larger than the value of 2.01 for the pure GO film with M_s value of 5.52×10^{-3} emu cm^{-3} in the LRS and 1.11×10^{-2} emu cm^{-3} in the HRS. The *M–H* curve was measured again after the GQDs:GO hybrid film in the HRS were exposed to the atmosphere for 28 days, with the result shown in Fig. 5(a). The M_{HRS} still reaches up to 2.34×10^{-2} emu cm^{-3}, preserving over 95% of the initial M_s in the HRS, implying excellent retention of magnetism. Most importantly, the magnetic property can be controlled reversibly during RS. The variations in the M_s value in the GQDs:GO hybrid film and GO film over three consecutive RS cycles are shown in Fig. 5(b). There is no appreciable reduction in magnetism and M_{HRS}/M_{LRS} for GQDs:GO hybrid film, whereas GO film retained only 71% of the initial M_{HRS}/M_{LRS} ratio after the third cycle. The M_s value of the GQDs:GO hybrid film at HRS was maintained 2.2 times higher than that of the GO film. Meanwhile the M_{HRS}/M_{LRS} of the former is still obviously 250% higher than the ratio of the latter in the three cycles. This indicates the excellent stability of magnetic modulation of the GQDs:GO hybrid film.

Fig. 6(a) shows a typical *I–V* curve plotted on a log–log scale. In the HRS, the I-V curve with linear behavior (slope ~1.03) and quadratic (slope ~2.11) was observed at low bias. The current subsequently rises rapidly with a slope of ~9.95 at high bias, indicating that the conduction mechanism conformed to space-charge-limited conduction (SCLC) [35,66]. In the LRS, the linear relation (slope ~0.99) of the *I–V* curve throughout the entire voltage-sweep region confirmed the ohmic conduction behaviour, implying that high conductivity was a confined filamentary effect in the LRS [66]. The trap density (N_t) can be calculated by the following equation [52,54,66],

$$N_t = \frac{2\varepsilon\varepsilon_0 V_{TFL}}{eL^2}, \quad (1)$$

where ε_0 (vacuum permittivity) and e (elementary charge) are constants, which are equal to 8.854×10^{-12} Fm^{-1} and 1.6×10^{-19}, respectively; ε represents the relative dielectric constant; L is the thickness of the dielectric layer; and V_{TFL}, the onset voltage of the trap filled limit, is 0.33 V in the HRS and close to 0 in the LRS, respectively, which are obtained from the plots of log*I*–log *V* shown in Fig. 6(a). By calculation, it is found that N_t is approximately 4.508×10^{16} cm^{-3} in the HRS, which is reduced obviously to around 0 in the LRS. It suggests that the trap densities (mainly oxygen groups of GO) can be eliminated significantly by setting the device into the LRS under an applied negative electric field, which is in agreement with the Raman spectrum results shown in Fig. 6(b). It can be seen that the D peak and G peak appear in both films near 1373 cm^{-1} and 1608 cm^{-1} [38], respectively. The value of I_D/I_G is proportional to the number of oxygen groups in the film [54]. I_D/I_G = 0.74 in the LRS, which is smaller than the corresponding value of 1.04 in the HRS. This indicates that most of the oxygen groups are eliminated from

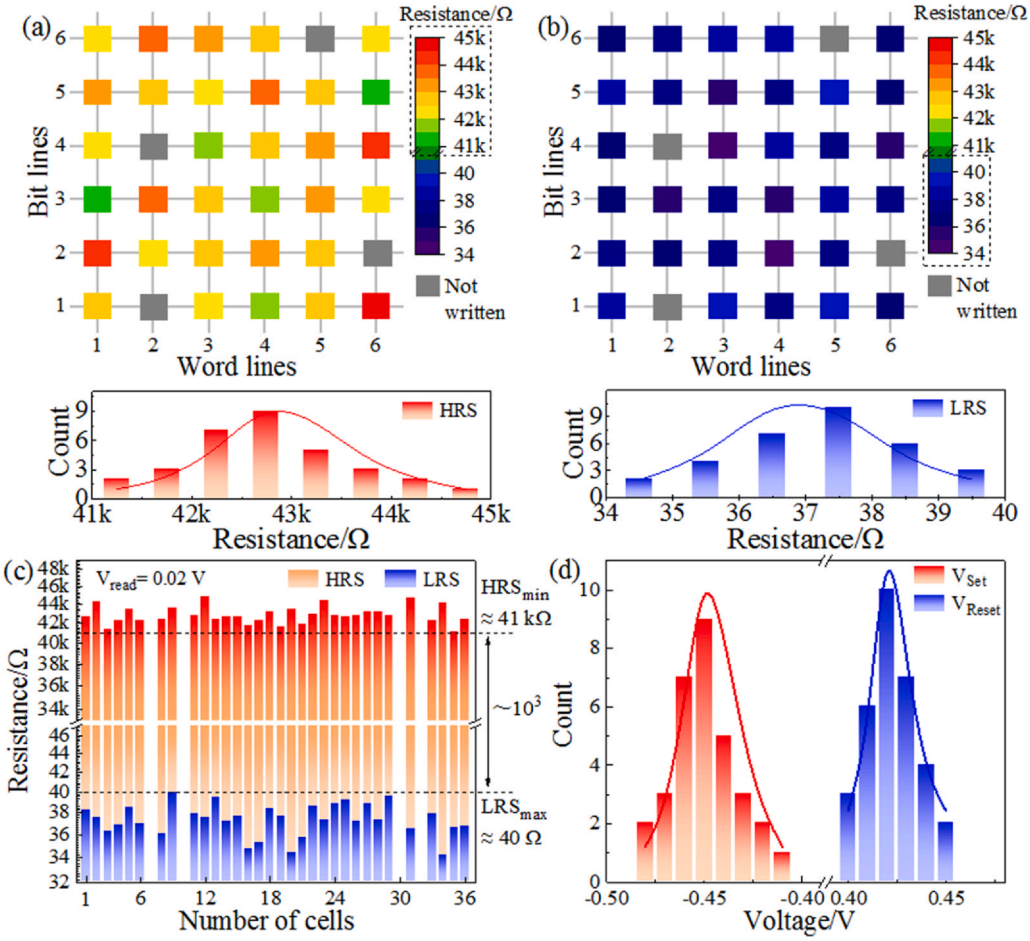

Fig. 4. Colour resistance map of the 36 memory cells in the (a) HRS and (b) LRS. The unwritten cells are displayed in grey. The resistance values (at the right) are given by colour scale bar. The resistance distributions (at the bottom) are displayed in histograms for each memory cell in the HRS (red) and LRS (blue). (c) Resistance values of the HRS (red) and LRS (blue) plotted for each memory cell. The blank spaces denote the unwritten cells. The minimum value in the HRS and maximum value in the LRS are indicated on the right. (d) Distributions of V_{SET} and V_{RESET} of 32 normal memory cells. (For interpretation of the references to colour in this figure legend, the reader is referred to the web version of this article.)

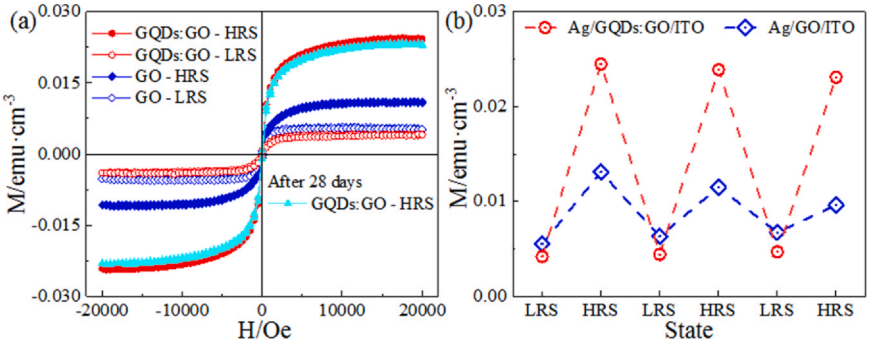

Fig. 5. Magnetism of GQDs:GO hybrid film and GO film at room temperature in the LRS and HRS. (a) *M–H* curves. (b) Reversible changes in the magnetic moment caused by RS behaviour.

the GQDs:GO hybrid film, or the enhancement of the sp^2 bond and the corresponding degradation of the sp^3 hybrid bond in the LRS. Conversely, the sp^2 clusters dominated in the LRS, whereas sp^2 was suppressed with conversion into sp^3 clusters in the HRS, which is in agreement with the results reported previously in the literature [38,67,68].

XPS was performed to obtain information on the change in chemical states in the HRS and LRS. The C1s core-level XPS spectra of the Ag/GQDs:GO/ITO device for HRS and LRS are displayed in Fig. 6(c). The C1s spectra in both states can be subdivided into three peaks by Gaussian fitting. The peaks attribute to the C–C (sp^2), C–O (epoxide), and C=O (carbonyl) at approximately 284.4, 286.5, and 288.3 eV, respectively [54–56]. Based on the areas of the corresponding fitting peaks, as shown in Table 1, it is clearly seen that the relative percentage of the C–C bond increased sharply to 88.2% in the LRS from 51.5% in the HRS, accompanied by a significant reduction (from 41.1% in the HRS to 5.7% in the LRS) in C–O groups. In contrast, there was no obvious variation observed in the C=O bonds between the two states. This means that oxygen groups (C–O rather than C=O) were mainly reduced when the GQDs:GO film set to the LRS. This is

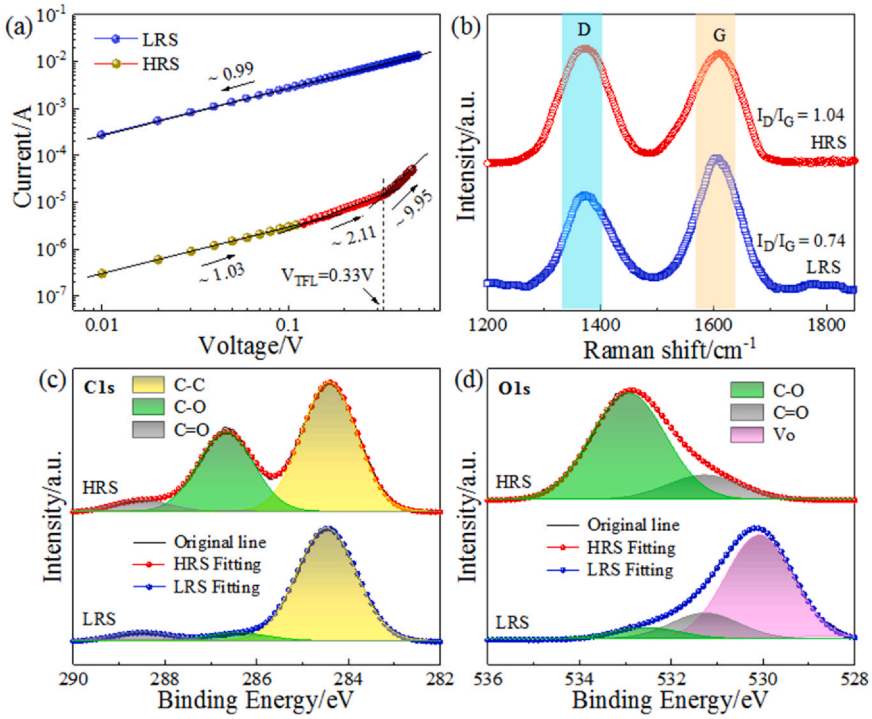

Fig. 6. (a) Linear fitting of the *I–V* curve of Ag/GQDs:GO/ITO device, plotted on a log–log scale. (b) Raman spectra, (c) C1s XPS spectra, and (d) O1s XPS spectra of GQDs:GO hybrid film in the HRS and LRS.

further confirmed by the O1s XPS measurement shown in Fig. 6(d). A new characteristic peak representing oxygen vacancy (Vo) appeared at 530.6 eV [69] after switching to the LRS by the application of a negative bias. As shown in Table 1, the C–O bonds, rather than C=O bonds, were mainly detached and large amounts (approximately 84.0%) of Vo were generated when the device was triggered to the LRS. This is in agreement with the Raman spectroscopy and C1s XPS results displayed in Fig. 6(b) and (c). It has been reported experimentally and theoretically [30] that only carbon atoms in the regions surrounded by epoxy groups (C–O–C) were able to hold a magnetic moment. Therefore, we speculate that the electrical and magnetic changes of the device might be related to the number of epoxy groups in the GO-based film.

Compared with the Ag/GO/ITO device without GQDs, high RS ratios and large magnetic modulation are demonstrated at low operating voltages in Ag/GQDs:GO/ITO resistive memories with the introduction of GQDs. It is deduced that the RS and magnetic modulation in the Ag/GQDs:GO/ITO device may be related to the charge transfer between GO and GQDs. Thus, the simplified energy-level structures of the Ag/GQDs:GO/ITO device were studied to further clarify the physical mechanism of RS and magnetism. According to previous reports [70,71], the work functions (W_F) of the Ag and ITO electrodes are −4.26 and −4.8 eV, respectively. To obtain the energy-level structures of GO and GQDs, UPS spectrum and UV–Vis absorption spectrum tests were conducted. For the UPS measurements, a He laser at an accelerating energy of 21.22 eV was used. As displayed in Fig. 7(a), the value of the secondary electron cut-off ($E_{cut\text{-}off}$) of GO is 17.37 eV (the Fermi level E_F is assumed to be 0 eV). According to the following equation [70],

$$W_F = 21.22 - (E_{cut-off} - E_F), \quad (2)$$

the W_F of GO is 3.85 eV. Considering that the highest occupied molecular orbital (HOMO) level cut-off ($E_{HOMO,\ cut\text{-}off}$) of GO is 2.55 eV (inset of Fig. 7a), the HOMO level of GO is calculated as −6.40 eV. Fig. 7(b) shows the UPS spectrum of the GQDs. It can be seen that $E_{cut\text{-}off}$ = 16.69 eV and E_{HOMO} = 1.53 eV. Based on the above calculation method, the W_F of the GQDs is 4.53 eV and the HOMO level is −6.06 eV. Fig. 7(c) and (d) show the UV–Vis absorption spectrum of GO and GQDs, from which the optical bandgap (E_g) is determined to be 3.12 and 2.69 eV, respectively, similar to previously reported value of ~3.3 [72]. and ~2.4 eV [73]. Therefore, the GO sample had a lowest unoccupied molecular orbital (LUMO) level of −3.28 eV, which is higher than the GQDs with a LUMO level of −3.37 eV.

It was impossible to form Ag CFs because Ag could not be reduced to Ag ions under a negative bias [54]. On the contrary, it was easy for the oxygen detached from the oxygen groups to capture electrons and become oxygen ions and migrate to the ITO BE from the GQDs:GO film under the application of a negative electric field. Based on the above results, the RS behaviours in the Ag/GQDs:GO/ITO device could be ascribed to the reversible formation and rupture of CFs composed of sp^2 clusters, similar to what was mentioned in the previous report [32,38], because of the migration of oxygen anions in GQDs:GO hybrid film under an electric field. The reversible

Table 1
Oxygen groups in the GQDs:GO film.

Resistance states	C1s			O1s		
	C–C (sp^2)	C–O (epoxy)	C=O (carbonyl)	C–O (epoxy)	C=O (carbonyl)	Vo
HRS (%)	51.5	41.1	7.4	88.5	11.5	0
LRS (%)	88.2	5.7	7.1	6.3	9.7	84.0

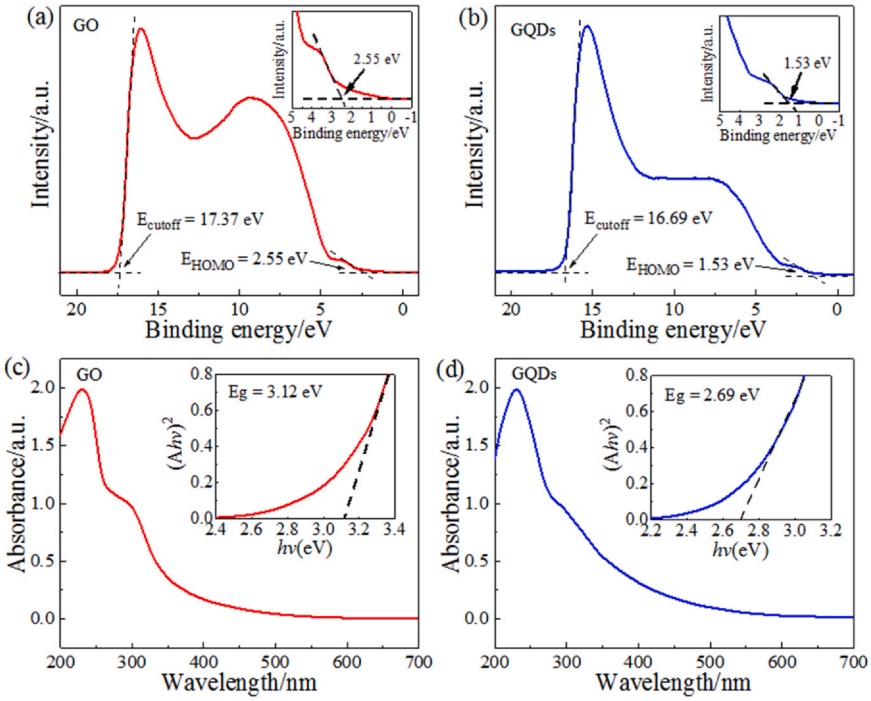

Fig. 7. UPS plot of (a) GO and (b) GQDs. The insets in (a) and (b) show the magnified views of the low-binding-energy region. UV–Vis absorption spectra of (c) GO and (d) GQDs. The insets in (c) and (d) show the Tauc plots.

migration of negatively charged oxygen anions leads to a change in the number of oxygen groups (mainly epoxy groups), resulting in strong and weak magnetic variations in the GQDs:GO hybrid film because C atoms in the region surrounded by epoxy groups hold a magnetic moment.

The mechanism for the electrical manipulation of RS and magnetism in GQDs:GO hybrid films is discussed in Fig. 8. A schematic diagram of the energy band of the Ag/GQDs:GO/ITO device under zero bias is shown in Fig. 8(a). The GO serves as the electron-blocking layer [74] owing to its wide energy gap (3.12 eV) compared with that of the GQDs (2.69 eV), and the difference between the energy levels of the GO and GQDs leads to the formation of potential wells as electron trapping and de-trapping centers [75]. A few epoxy groups are located uniformly in the GQDs:GO film, as illustrated in Fig. 8(d). Highly conductive sp^2 regions were interrupted by low-conductivity sp^3 domains, leading to high resistance in the IS. Only a small fractional amount of unpaired spin in the carbon atoms surrounded by epoxy groups (called carbon radicals) [76] from a cluster, such as region I in Fig. 8(g), was generated, resulting in the film showing weak magnetism at room temperature (Fig. S4 in the Supporting Information).

When a negative voltage bias was applied to the Ag TE, the energy band would bend [70], as displayed in Fig. 8(b). Many electrons from the Ag TE were injected into the dielectric layer. Simultaneously, the oxygen from the epoxy groups could trap those injected electrons and become isolated oxygen anions (no bonding with carbon atoms) and migrate to the ITO BE, leading to high resistivity of the sp^3 domains converted to sp^2 carbon clusters. Here, GQDs with high effects of local electric fields [40,48] provided good chemical linkage to connect the local sp^2 clusters together, forming local high-conductivity filamentary tracks, thus switching the devices from the HRS to LRS without forming process, as displayed in Fig. 8(e). At that time, the GQDs:GO film displayed a lower magnetism than that in the IS, as only a few sp^3 domains of the epoxy groups were left, as illustrated in Fig. 8(h). Notably, it was the insertion of GQDs that, similar to shortening the distance between pure GO layers, reduced the dispersion of the random formation of sp^2 CFs, which was responsible for the lower operating voltages and more stable RS (as shown in Fig. 3), compared with the Ag/GO/ITO device without GQDs.

When a reverse voltage was applied, the trapped electrons were extracted from the trapping centres, and many more oxygen anions than those migrating to ITO moved into the GQDs:GO hybrid film from the ITO BE, owing to its high oxygen reservoirs [77] and strong oxygen adsorption of GQDs. This led to the continuous creation of many more low-conductive sp^3 areas in the GQDs:GO hybrid film than in IS (see Fig. 8c). The highly conductive sp^2 regions were interrupted again by sp^3 domains, resulting in the rupture of the sp^2 CFs, transforming the device into HRS again, as shown in Fig. 8(f). With the increase and redistribution of the surrounding epoxy groups, more carbon radicals were formed in the GQDs:GO film. In other words, the unpaired spins in the carbon $2p_z$ orbitals orthogonal to oxygen 2p are arranged in parallel, forming local magnetic moment, as observed in regions I, II and III in Fig. 8(i), and finally producing magnetic behaviours [30]. Simultaneously it is speculated that the exchange coupling effect could happen between those adjacent local magnetic moments, especially in the GQDs, mediated by the oxygen 2p in the epoxy groups, producing magnetic ordering [78]. Thus, a strong global magnetic moment appeared in the films at room temperature, which was greater than that of the IS and LRS.

4. Conclusions

Large-magnitude magnetic modulation and low operating voltages were obtained in Ag/GQDs:GO/ITO resistive memories. The RS ratios and saturation magnetization (M_s) of GQDs memristor are demonstrated approximately 20 and 2.2 times higher than that of GQDs-free memristor, respectively. The electron orbital hybridization of carbon atom transition from sp^2 to sp^3 is induced by reversible oxygen anions migrations, which create resistive and magnetic switching bifunctional effect. GQDs under the effect of a local electric field contributed to the development of sp^2 filaments along the GQDs, thus reducing the dispersion of the random formation of CFs. Most importantly, GQDs contribute the same

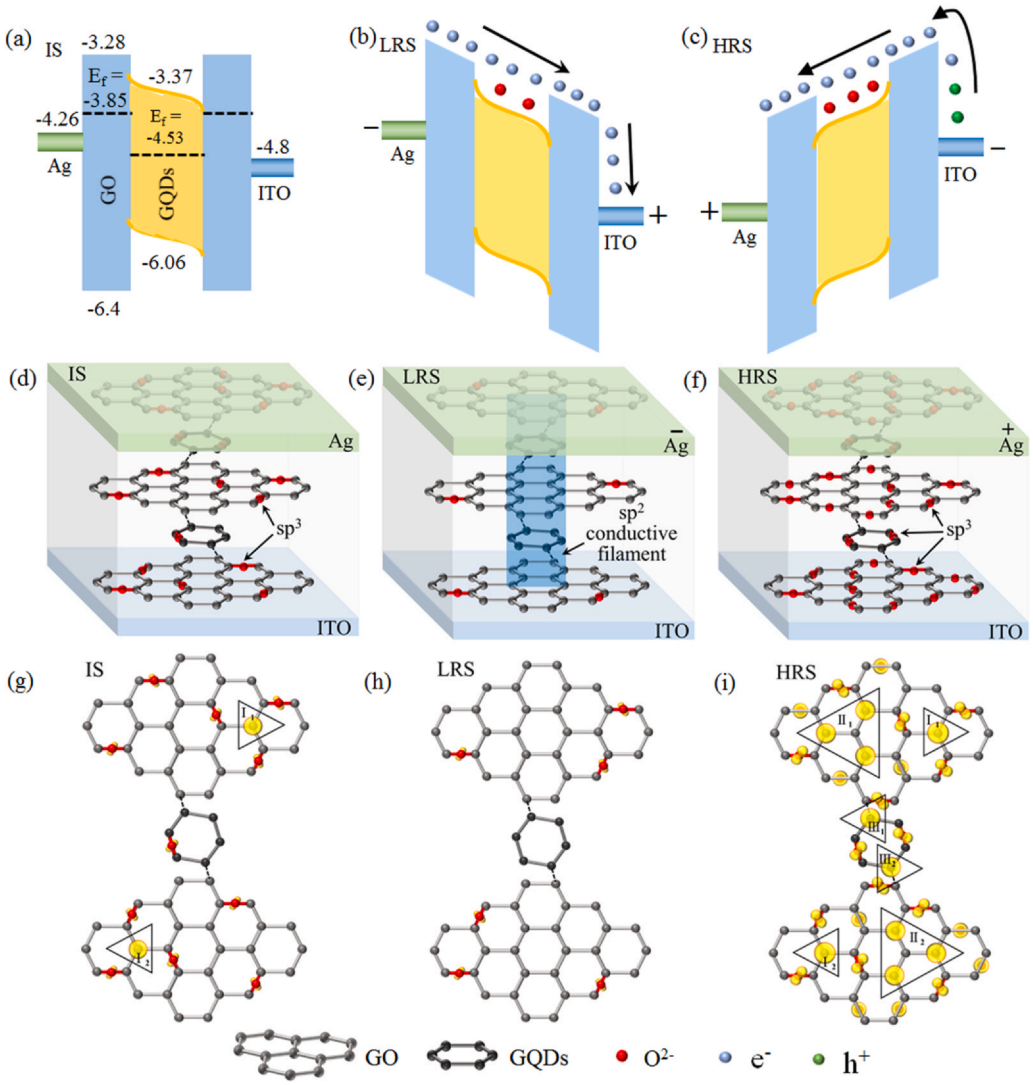

Fig. 8. Energy band schematic diagram of Ag/GQDs:GO/ITO device in (a) IS, (b) LRS, and (c) HRS; molecular diagram of Ag/GQDs:GO/ITO device in (d) IS, (e) LRS, and (f) HRS; and microscopic diagram showing linking regions in (g) IS, (h), LRS, and (i) HRS.

magnetic ordering for the local separate magnetic moment, producing global magnetic behaviour in the GQDs:GO hybrid film in the HRS at room temperature. Our research paves a way for GO-based bifunctional memristive devices with high resistive memories and large magnetic modulation, exploring the application in high-density information storage.

CRediT authorship contribution statement

Ren S, Zhao J and Cao G conceived and supervised the project. Li Z prepared the samples under the guidance of Ren S. Li Z and Liu M performed test characterization and analyzed data under the guidance of Ren S and Zhao J. Ren S wrote the manuscript and all authors participated in the revision and discussion.

Declaration of Competing Interest

The authors declare that they have no known competing financial interests or personal relationships that could have appeared to influence the work reported in this paper.

Acknowledgements

We acknowledge National Natural Science Foundation of China (11772207, 11790282 and U1534204); Natural Science Foundation of Hebei Province (A2018210123); Natural Science Foundation of Hebei Province for Distinguished Young Scholar (A2019210204); Natural Science Foundation of Hebei Education Department (ZD2020192); Youth Top-Notch Talents Supporting Plan of Hebei Province; State Key Laboratory of Mechanics and Control of Mechanical Structures, Nanjing University of Aeronautics and Astronautics (MCMS-E-0519G04).

Appendix A. Supporting information

Supplementary data associated with this article can be found in the online version at doi:10.1016/j.jallcom.2020.158339.

References

[1] T.C. Chang, K. Chang, T. Tsai, T. Chu, S.M. Sze, Resistance random access memory, Mater. Today 19 (2016) 254–264.
[2] M.J. Lee, S. Seo, D.C. Kim, S.E. Ahn, D.H. Seo, A low-temperature-grown oxide diode as a new switch element for high-density, nonvolatile memories, Adv. Mater. 19 (2007) 73–76.

[3] G.I. Meijer, Who wins the nonvolatile memory race? Science 319 (2008) 625–1626.
[4] W.H. Xue, G. Liu, Z.C. Zhong, Y.H. Dai, J. Shang, A 1D vanadium dioxide nanochannel constructed via electric-field-induced ion transport and its superior metal-insulator transition, Adv. Mater. 29 (2017) 1702162.
[5] S.X. Ren, L.Z. Tang, Q. Sun, Z.H. Li, H.F. Yang, Resistive switching and magnetism in transparent a-TiOx films deposited by magnetron sputtering, J. Alloy. Compd. 763 (2018) 638–642.
[6] J.J. Guo, L.Q. Wu, S.X. Ren, X. Kang, W. Chen, Ultra-low voltage control of magnetic properties in amorphous MgO, Appl. Phys. Lett. 111 (2017) 192402.
[7] X. Kang, Y.J. Gao, L.F. Liu, W. Chen, X. Zhao, Enhanced magnetic modulation in NiO-based memory device through ionic liquid pre-treatment, Appl. Phys. Lett. 115 (2019) 103501.
[8] T.W. Hickmott, Low-frequency negative resistance in thin anodic oxide films, J. Appl. Phys. 33 (1962) 2669–2682.
[9] F. Matsukura, Y. Tokura, H. Ohno, Control of magnetism by electric fields, Nat. Nanotechnol. 10 (2015) 209–220.
[10] D.N. Matsukevich, A. Kuzmich, Quantum state transfer between matter and light, Science 306 (2004) 663–666.
[11] N. Tombros, C. Jozsa, M. Popinciuc, H.T. Jonkman, B.J. van Wees, Electronic spin transport and spin precession in single graphene layers at room temperature, Nature 448 (2007) 571–574.
[12] T.Y. Yang, J. Balakrishnan, F. Volmer, A. Avsar, M. Jaiswal, Observation of long spin-relaxation times in bilayer graphene at room temperature, Phys. Rev. Lett. 107 (2011) 047206.
[13] O.V. Yazyev, M.I. Katsnelson, Magnetic correlations at graphene edges: basis for novel spintronics devices, Phys. Rev. Lett. 100 (2008) 047209.
[14] D.W. Lee, J.W. Seo, Magnetic frustration of graphite oxide, Sci. Rep. 7 (2017) 44690.
[15] J.J. Palacios, J. Fernández-Rossier, L. Brey, Vacancy-induced magnetism in graphene and graphene ribbons, Phys. Rev. B 77 (2008) 195428.
[16] Y.W. Ma, Y.H. Lu, J.B. Yi, Y.P. Feng, T.S. Herng, Room temperature ferromagnetism in teflon due to carbon dangling bonds, Nat. Commun. 3 (2012) 727.
[17] C. Hontoria-Lucas, A.J. López-Peinado, J.D. López-González, M.L. Rojas-Cervantes, R.M. Martín-Aranda, Study of oxygen-containing groups in a series of graphite oxides: physical and chemical characterization, Carbon 33 (1995) 1585–1592.
[18] J.P. Rourke, P.A. Pandey, J.J. Moore, M. Bates, I.A. Kinloch, The real graphene oxide revealed: stripping the oxidative debris from the graphene-like sheets, Angew. Chem. Int. Ed. 50 (2011) 3173–3177.
[19] X. Leng, R.T. Liu, J.P. Zou, X. Xiong, H.W. He, Tuning microstructure and surface chemistry of reduced graphene oxide by mild reduction, J. Central South Univ. 23 (2016) 1823–1830.
[20] X.B. Yan, L. Zhang, H.W. Chen, X.Y. Li, P. Zhou, Graphene oxide quantum dots based memristors with progressive conduction tuning for artificial synaptic learning, Adv. Funct. Mater. 28 (2018) 1803728.
[21] D.W. Lee, J.W. Seo, G.R. Jelbert, L. de Los Santos, J.M. Cole, Transparent and flexible polymerized graphite oxide thin film with frequency-dependent dielectric constant, Appl. Phys. Lett. 95 (2009) 172901.
[22] D.W. Lee, X.Q. Zou, X. Zhu, J.W. Seo, J.M. Cole, Ultrafast carrier phonon dynamics in NaOH-reacted graphite oxide film, Appl. Phys. Lett. 101 (2012) 021604.
[23] D.W. Lee, J.W. Seo, X. Zhu, J. Lee, H.-J. Shin, Quantum confinement-induced tunable exciton states in graphene oxide, Sci. Rep. 3 (2013) 2250.
[24] T. Tang, F.C. Liu, Y. Liu, X.Y. Li, Q.H. Xu, Identifying the magnetic properties of graphene oxide, Appl. Phys. Lett. 104 (2014) 123104.
[25] E.J.G. Santos, A. Ayuela, D. Sánchez-Portal, Universal magnetic properties of sp3-type defects in covalently functionalized graphene, New J. Phys. 14 (2012) 043022.
[26] M. Wang, W. Huang, M.B. Chan-Park, C.M. Li, Magnetism in oxidized graphenes with hydroxyl groups, Nanotechnology 22 (2011) 105702.
[27] T. Tang, N.J. Tang, Y.P. Zheng, X.G. Wan, Y. Liu, Robust magnetic moments on the basal plane of the graphene sheet effectively induced by OH groups, Sci. Rep. 5 (2015) 8448.
[28] S.C. Ray, N. Soin, T. Makgato, C.H. Chuang, W.F. Pong, Graphene supported graphone/graphane bilayer nanostructure material for spintronics, Sci. Rep. 4 (2014) 3862.
[29] Y.F. Wang, S.B. Singh, M.V. Limaye, Y.C. Shao, S.H. Hsieh, Visualizing chemical states and defects induced magnetism of graphene oxide by spatially-resolved-X-ray microscopy and spectroscopy, Sci. Rep. 5 (2015) 15439.
[30] D.W. Lee, J.W. Seo, X. Zhu, J.M. Cole, H.B. Su, Magnetism in graphene oxide induced by epoxy groups, Appl. Phys. Lett. 106 (2015) 172402.
[31] G. Eda, G. Fanchini, M. Chhowalla, Large-area ultrathin films of reduced graphene oxide as a transparent and flexible electronic material, Nat. Nanotechnol. 3 (2008) 270–274.
[32] H.Y. Jeong, J.Y. Kim, J.W. Kim, J.O. Hwang, J.-E. Kim, Graphene oxide thin films for flexible nonvolatile memory applications, Nano Lett. 10 (2010) 4381–4386.
[33] A. Rani, D.B. Velusamy, F. Marques Mota, Y.H. Jang, R.H. Kim, One-step all-solution-based Au–GO core–shell nanosphere active layers in nonvolatile ReRAM devices, Adv. Funct. Mater. 27 (2017) 1604604.
[34] A. Rani, D.B. Velusamy, R.H. Kim, K. Chung, F.M. Mota, Non-volatile ReRAM devices based on self-assembled multilayers of modified graphene oxide 2D nanosheets, Small 12 (2016) 6167–6174.
[35] F. Zhuge, B.L. Hu, C.L. He, X.F. Zhou, Z.P. Liu, Mechanism of nonvolatile resistive switching in graphene oxide thin films, Carbon 49 (2011) 3796–3802.
[36] S.K. Kim, J.Y. Kim, B.C. Jang, M.S. Cho, S.Y. Choi, Conductive graphitic channel in graphene oxide-based memristive devices, Adv. Funct. Mater. 26 (2016) 7406–7414.
[37] J.Q. Liu, Z.Y. Yin, X.H. Cao, F. Zhao, L.H. Wang, Fabrication of flexible, all-reduced graphene oxide non-volatile memory devices, Adv. Mater. 25 (2013) 233–238.
[38] G. Khurana, P. Misra, R.S. Katiyar, Forming free resistive switching in graphene oxide thin film for thermally stable nonvolatile memory applications, J. Appl. Phys. 114 (2013) 124508.
[39] K. Sungkyu, H.J. Jung, C. Kim Jong, K.S. Lee, S.S. Park, V.P. Dravid, K. He, H.Y. Jeong, In situ observation of resistive switching in an asymmetric graphene oxide bilayer structure, ACS Nano 12 (2018) 7335–7342.
[40] X.B. Yan, L. Zhang, Y.Q. Yang, Z.Y. Zhou, J.H. Zhao, Highly improved performance in $Zr_{0.5}Hf_{0.5}O_2$ films inserted with graphene oxide quantum dots layer for resistive switching non-volatile memory, J. Mater. Chem. C 5 (2017) 11046–11052.
[41] K.A. Ritter, J.W. Lyding, The influence of edge structure on the electronic properties of graphene quantum dots and nanoribbons, Nat. Mater. 8 (2009) 235–242.
[42] L. Wang, Y.L. Wang, T. Xu, H.B. Liao, C.J. Yao, Gram-scale synthesis of single-crystalline graphene quantum dots with superior optical properties, Nat. Commun. 5 (2014) 5357.
[43] L.L. Li, G.H. Wu, G.H. Yang, J. Peng, J.W. Zhao, Focusing on luminescent graphene quantum dots: current status and future perspectives, Nanoscale 5 (2013) 4015–4039.
[44] C.H. Wang, W. He, Y. Tong, Y.S. Zhang, K.J. Huang, Memristive devices with highly repeatable analog states boosted by graphene quantum dots, Small 13 (2017) 1603435.
[45] S. Neubeck, L.A. Ponomarenko, F. Freitag, A.J.M. Giesbers, U. Zeitler, From one electron to one hole: quasiparticle counting in graphene quantum dots determined by electrochemical and plasma etching, Small 6 (2010) 1469–1473.
[46] C. Bostedt, T.V. Buuren, T.M. Willey, N. Franco, L.J. Terminello, Strong quantum-confinement effects in the conduction band of germanium nanocrystals, Appl. Phys. Lett. 84 (2004) 4056–4058.
[47] R. Sako, H. Hosokawa, H. Tsuchiya, S. Member, Computational study of edge configuration and quantum confinement effects on graphene nanoribbon transport, IEEE Electron Device Lett. 32 (2011) 6–8.
[48] T. Chen, Y.J. Gao, W. Chen, X. Zhao, Improved resistive memory based on ZnO–graphene hybrids through redox process of graphene quantum dots, Phys. Status Solidi RRL 13 (2019) 1900153.
[49] C.M. Jia, X.Y. Zhao, Y.H. Lai, J.J. Zhao, P.C. Wang, Highly flexible, robust, stable and high efficiency perovskite solar cells enabled by van der Waals epitaxy on mica substrate, Nano Energy 60 (2019) 476–484.
[50] G.Z. Xia, B.Y. Huang, Y. Zhang, X.Y. Zhao, J.J. Zhao, Nanoscale insights into photovoltaic hysteresis in triple-cation mixed-halide perovskite: resolving the role of polarization and ionic migration, Adv. Mater. 31 (2019) 1902870.
[51] R. Chen, W. Wang, T. Bu, Z.L. Ku, J. Zhong, Y. Peng, S.Q Xiao, W. You, F.Z. Huang, Y.B. Cheng, Z.Y. Fu, Low-cost fullerene derivative as an efficient electron transport layer for planar perovskite solar cells, Acta Phys. Chim. Sin. 35 (2019) 401–407.
[52] T. Kavinkumar, D. Sastikumar, S. Manivannan, Effect of functional groups on dielectric, optical gas sensing properties of graphene oxide and reduced graphene oxide at room temperature, RSC Adv. 5 (2015) 10816–10825.
[53] F. Liu, M.H. Jang, H.D. Ha, J.H. Kim, Y.H. Cho, Facile synthetic method for pristine graphene quantum dots and graphene oxide quantum dots: origin of blue and Green Luminescence, Adv. Mater. 25 (2013) 3657–3662.
[54] S.X. Ren, Z.H. Li, L.Z. Tang, X. Su, J.J. Zhao, Conduction response in highly flexible nonvolatile memory devices, Adv. Electron. Mater. 6 (2020) 2000151.
[55] R. Arul, R.N. Oosterbeek, J. Robertson, G.Y. Xu, J.Y. Jin, The mechanism of direct laser writing of graphene features into graphene oxide films involves photoreduction and thermally assisted structural rearrangement, Carbon 99 (2016) 423–431.
[56] J.R. Rani, J. Oh, J. Park, J. Lim, B. Park, Controlling the luminescence emission from palladium grafted graphene oxide thin films via reduction, Nanoscale 5 (2013) 5620–5627.
[57] J.R. Rani, S.I. Oh, J.M. Woo, J.H. Jang, Low voltage resistive memory devices based on graphene oxide–iron oxide hybrid, Carbon 94 (2015) 362–368.
[58] Z.L. Hu, Y.F. Chen, Q.L. Hou, R.M. Yin, F.S. Liu, Characterization of graphite oxide after heat treatment, New J. Chem. 36 (2012) 1373–1377.
[59] J.T. Chen, Y.J. Fu, Q.F. An, S.C. Lo, S.H. Huang, Tuning nanostructure of graphene oxide/polyelectrolyte LbL assemblies by controlling pHof GO suspension to fabricate transparent and super gas barrier films, Nanoscale 5 (2013) 9081–9088.
[60] Y. Li, Y. Zhao, H.H. Cheng, Y. Hu, G.Q. Shi, Nitrogen-doped graphene quantum dots with oxygen-rich functional groups, J. Am. Chem. Soc. 134 (2012) 15–18.
[61] J.J. Guo, S.X. Ren, L.Q. Wu, X. Kang, W. Chen, Low-power, high-uniform, and forming-free resistive memory based on Mg-deficient amorphous MgO film with rough surface, Appl. Surf. Sci. 434 (2018) 1074–1078.
[62] A. Sawa, Resistive switching in transition metal oxides, Mater. Today 11 (2008) 28–36.
[63] X.N. Zhao, Z.Q. Wang, X. Yu, H.Y. Xu, J.X. Zhu, Photocatalytic reduction of graphene oxide-TiO_2 nanocomposites for improving resistive-switching memory behaviors, Small 14 (2018) 1801325.
[64] P. Saini, M. Singh, J. Thakur, R.A. Patil, Y.-R. Ma, Probing the mechanism for bipolar resistive switching in annealed graphene oxide thin films, ACS Appl. Mater. Interfaces 10 (2018) 6521–6530.
[65] S.X. Ren, G.W. Sun, J. Zhao, J.Y. Dong, Y. Wei, Electric field-induced magnetic switching in Mn:ZnO film, Appl. Phys. Lett. 104 (2014) 232406.
[66] Y.Q. Zhang, X.T. Liu, P.W. Li, Y.Y. Duan, X.T. Hu, Dopamine-crosslinked TiO_2/perovskite layer for efficient and photostable perovskite solar cells under full spectral continuous illumination, Nano Energy 56 (2018) 733–740.

[67] J. Chen, Y.R. Li, L. Huang, C. Li, G.Q. Shi, High-yield preparation of graphene oxide from small graphite flakes via an improved Hummers method with a simple purification process, Carbon 81 (2015) 826–834.
[68] B. Yu, X. Wang, X.D. Qian, W.Y. Xing, H.Y. Yang, Functionalized graphene oxide/phosphoramide oligomer hybrids flame retardant prepared via in situ polymerization for improving the fire safety of polypropylene, RSC Adv. 4 (2014) 31782–31794.
[69] S. Baek, J. Song, S. Lim, Improvement of the optical properties of ZnO nanorods by Fe doping, Phys. B Condens. Matter 399 (2007) 101–104.
[70] L.Q. Wu, J.J. Guo, W. Zhong, W.J. Zhang, X. Kang, Flexible, multilevel, and low-operating-voltage resistive memory based on MoS_2-rGO hybrid, Appl. Surf. Sci. 463 (2019) 947–952.
[71] S.C. Lim, J.H. Jang, D.J. Bae, G.H. Han, S. Lee, Contact resistance between metal and carbon nanotube interconnects: effect of work function and wettability, Appl. Phys. Lett. 95 (2009) 264103.
[72] T.F. Yeh, J.M. Syu, C. Cheng, T.H. Chang, H. Teng, Graphite oxide as a photocatalyst for hydrogen production from water, Adv. Funct. Mater. 20 (2010) 2255–2262.
[73] R.Q. Ye, Z.W. Peng, A. Metzger, J. Lin, J.A. Mann, Bandgap engineering of coal-derived graphene quantum dots, ACS Appl. Mater. Interfaces 7 (2015) 7041–7048.
[74] D.L. Wang, F.Z. Ji, X.M. Chen, Y. Li, B.F. Ding, Quantum conductance in MoS_2 quantum dots-based nonvolatile resistive memory device, Appl. Phys. Lett. 110 (2017) 093501.
[75] G.H. Shin, C.K. Kim, G.S. Bang, J.Y. Kim, B.C. Jang, Multilevel resistive switching nonvolatile memory based on MoS_2 nanosheet-embedded graphene oxide, 2D Mater. 3 (2016) 034002.
[76] X. Zhu, H. Su, Magnetism in hybrid carbon nanostructures: nanobuds, Phys. Rev. B 79 (2009) 165401.
[77] H.Y. Wu, C.C. Lin, C.H. Lin, Characteristics of graphene-oxide-based flexible and transparent resistive switching memory, Ceram. Int. 41 (2015) S823–S828.
[78] P. Schlottmann, Double-exchange mechanism for CrO_2, Phys. Rev. B 67 (2003) 174419.